Statistical analysis of wave propagation properties of equatorial noise observed at low altitudes

Miroslav Hanzelka[1,2], František Němec[2], Ondřej Santolík[1,2], Michel Parrot[3]

[1]Department of Space Physics, Institute of Atmospheric Physics of the Czech Academy of Sciences, Prague, Czech Republic

[2]Faculty of Mathematics and Physics, Charles University, Prague, Czech Republic

[3]LPC2E/CNRS, Orléans, France

Key Points:

- We present statistical analysis of wave propagation properties of equatorial noise observed at low altitudes by the DEMETER spacecraft
- The wave propagation properties are explained by 3D ray tracing simulations in a cold plasma
- Comparison of the spacecraft observations and ray statistics suggests a narrow distribution of wave normal angles in the source

Corresponding author: M. Hanzelka, mha@ufa.cas.cz

Abstract

Equatorial noise is an electromagnetic emission with line spectral structure, predominantly located in the vicinity of the geomagnetic equatorial plane at radial distances ranging from 2 to 8 Earth's radii. Here we focus on the rare events of equatorial noise occurring at ionospheric altitudes during periods of strongly increased geomagnetic activity. We use multicomponent electromagnetic measurements from the entire 2004–2010 DEMETER spacecraft mission and present a statistical analysis of wave propagation properties. We show that, close to the Earth, these emissions experience a larger spread in latitudes than they would at large radial distances and that their wave normals can significantly deviate from the direction perpendicular to local magnetic field lines. These results are compared to ray tracing simulations, in which whistler mode rays with initially nearly perpendicular wave vectors propagate down to the low altitudes with wave properties corresponding to the observations. We perform nonlinear fitting of the simulated latitudinal distribution of incident rays to the observed occurrence and estimate the distribution of wave normal angles in the source. The assumed Gaussian distribution provides the best fit with a standard deviation of 2° from the perpendicular direction. Ray tracing analysis further shows that small initial deviations from the meridional plane can rapidly increase during the propagation and result in deflection of the emissions before they can reach the altitudes of DEMETER.

Plain Language Summary

We study the electromagnetic emission called equatorial noise, which occurs frequently in the magnetosphere of Earth and is known to have an impact on the radiation belt dynamics. Here we present statistics of the rare events when the emissions reached the altitudes of 700 km and were detected by the low orbiting satellite DEMETER. Our analysis reveals an unusually high spread of recorded events in the latitude, and we also notice large deviations of the wave vector from the perpendicular direction. The observed wave properties and indices of geomagnetic activity are used to set up a ray tracing simulation. We confirm that the observations agree with the theoretical propagation properties of rays in the whistler mode, which is the wave mode associated with equatorial noise. The correspondence between simulation and observation is further improved by inferring the initial wave properties in the source with the help of nonlinear least-squares fitting. Additional simulations of ray propagation with nonzero initial deviation from the

plane of local meridian confirm that such deviations must be minimal; otherwise, the rays become deflected before reaching the altitude of the DEMETER satellite.

1 Introduction

Equatorial noise (EN) is one of the most intense natural electromagnetic emissions in the inner magnetosphere, occurring very often within several degrees around the geomagnetic equator and propagating in the whistler mode with extraordinary polarization (Santolík, Pickett, Gurnett, Maksimovic, & Cornilleau-Wehrlin, 2002). This mode of propagation implies a nearly linear polarization of the magnetic field fluctuations (Santolík et al., 2004). The equatorial noise emissions can play a significant role in controlling the distribution of energetic electrons in the radiation belts (Horne et al., 2007). EN is detected mostly in the frequency range from a few hertz up to about 1 kHz, and it can be commonly observed at radial distances ranging from $2\,R_{\mathrm{E}}$ (Earth's radii) up to about $8\,R_{\mathrm{E}}$ (Ma et al., 2013; Němec, Santolík, Pickett, Hrbáčková, & Cornilleau-Wehrlin, 2013; Posch et al., 2015; Hrbáčková et al., 2015). The first observation of EN dates back to the late 1960s when Russell et al. (1970) reported a new type of noise-like emissions measured by the OGO 3 satellite in the vicinity of the geomagnetic equator. It was later shown by Gurnett (1976), who analyzed the time-frequency spectrograms recorded onboard the Hawkeye 1 and Imp 6 spacecraft, that the spectrum of EN emissions consists of a complex superposition of harmonically spaced spectral lines. Despite this characteristic fine structure, the term equatorial "noise" is kept here for continuity reasons.

Perraut et al. (1982) noted that the spacing of spectral lines in the fine structure of EN is closely related to the local proton gyrofrequency f_{cp} in the EN source region and hypothesized that the emissions originate from the unstable ion ring distribution, which was observed simultaneously with an EN emission by the two GEOS spacecraft. This idea was further elaborated by several other authors (Boardsen et al., 1992; Meredith et al., 2008; Xiao et al., 2013) and has steadily become the prevailing theory for explaining the physical origin of equatorial noise. Growth rate simulations of ion Bernstein modes with Gaussian ring distributions (Horne et al., 2000; Liu et al., 2011; Ma et al., 2014; Chen, 2015) and partial shell proton distributions centered at a pitch angle of 90° (Min & Liu, 2016) show large growth peaks at multiples of the proton gyrofrequency with the upper frequency limit set by the lower hybrid frequency f_{lh}. Subsequent propagation in the whistler mode is then assumed.

The conversion from ion Bernstein modes with wave vectors nearly perpendicular to the local magnetic field lines has implications for the wave propagation characteristics of the EN. Perpendicular whistler mode waves starting in the equatorial region propagate both azimuthally and radially (Kasahara et al., 1994; Santolík, Pickett, Gurnett, Maksimovic, & Cornilleau-Wehrlin, 2002). During inward radial motion they may reach low altitudes, as was shown in the case study by Santolík et al. (2016) and statistical analysis of storm time EN events by Němec et al. (2016), both of which are based on DEMETER spacecraft measurements. The low frequency part of the emissions cannot propagate further down to the Earth's surface due to a cutoff in their mode structure, which is situated between f_{cp} and the O^+ ion gyrofrequency f_{cO}. During the propagation through the plasmasphere, the wave vectors remain nearly perpendicular to the ambient Earth's magnetic field (Boardsen et al., 2016), yet they are not restricted to any particular azimuthal direction (Němec, Santolík, Pickett, Hrbáčková, & Cornilleau-Wehrlin, 2013). It has been suggested by Santolík et al. (2016) that only those emissions that are confined close to the meridional plane can propagate down to the altitudes of DEMETER.

In this article, we present statistics of low altitude EN events found in the burst mode data gathered by the DEMETER spacecraft. We focus on the wave propagation properties and latitudinal and frequency distributions of these emissions. The observational results and the methods used to obtain them are presented in Section 2. The observed properties of EN are compared to statistics obtained from ray tracing simulations in a cold plasma, which is the main topic of Section 3. We assume purely meridional propagation (Section 3.2) and use minimization methods to estimate the distribution of wave normal angles and frequencies in the source that produces the best nonlinear least-squares fit of the latitudinal distribution of incident rays to the experimental data. Deviations of wave vectors from the meridional plane and the expected effect of azimuthal propagation on EN properties is analyzed separately in Section 3.3. In Sections 4 and 5 we discuss the impact of the thresholds applied in data processing, the choice of our simulation setup and the significance of our results, and we conclude with suggestions for the direction of future research.

2 Satellite Observation

2.1 Dataset and Processing Methods

The data used in the wave analysis were acquired by the ICE (system of four electrical sensors) and IMSC (triaxial set of magnetic sensors) instruments onboard the DEMETER spacecraft – see Berthelier et al. (2006) and Parrot et al. (2006) for a detailed description of these instruments. The spacecraft was operational from June 2004 to December 2010. It followed a nearly sun-synchronous circular orbit, altering between approximately 10:30 MLT and 22:30 MLT, and kept an altitude of about 710 km, later (December 2005) changed to 660 km. In the survey mode, DEMETER provided continuous wave measurements with one electric and one magnetic field component in a frequency range up to 20 kHz. More detailed data were available in the burst mode, which was triggered only in preselected regions, mostly at lower geomagnetic latitudes (Němec et al. (2007), Figure 1). Moreover, the burst mode provided waveforms of all six electromagnetic components measured with a sampling frequency of 2500 Hz, corresponding to a Nyquist frequency of 1250 Hz. With these waveforms, we can perform a detailed analysis of wave polarization and propagation properties using the singular value decomposition (SVD) methods described by Santolík et al. (2006).

In the burst mode data gathered over the 6.5 years of DEMETER operations, we found 46 EN emission events, 29 of them on the dayside and 17 on the nightside. These events were picked manually by identifying the line structure in the electric and magnetic spectra. The processed spectra of an example dayside event recorded on 2004-11-09 between 08:19:15 and 08:21:15 UT are presented in Figure 1, similar to the case analyzed by Santolík et al. (2016). In the electric and magnetic power spectrograms in Figures 1a and 1b, intense line emissions are discernible. Visual inspection of these lines shows that the spacing is approximately 20 Hz to 25 Hz, which corresponds to proton gyrofrequencies found at equatorial distances between 2.6 and 2.8 R_E if the dipole model of the geomagnetic field is assumed. This is the estimated location of the source region for this event. High values of wave magnetic field planarity parameter (Figure 1c), which measures the validity of the plane wave assumption made in the SVD analysis (Santolík et al., 2003), confirm that we are dealing with plane waves with low intensity noise in the background.

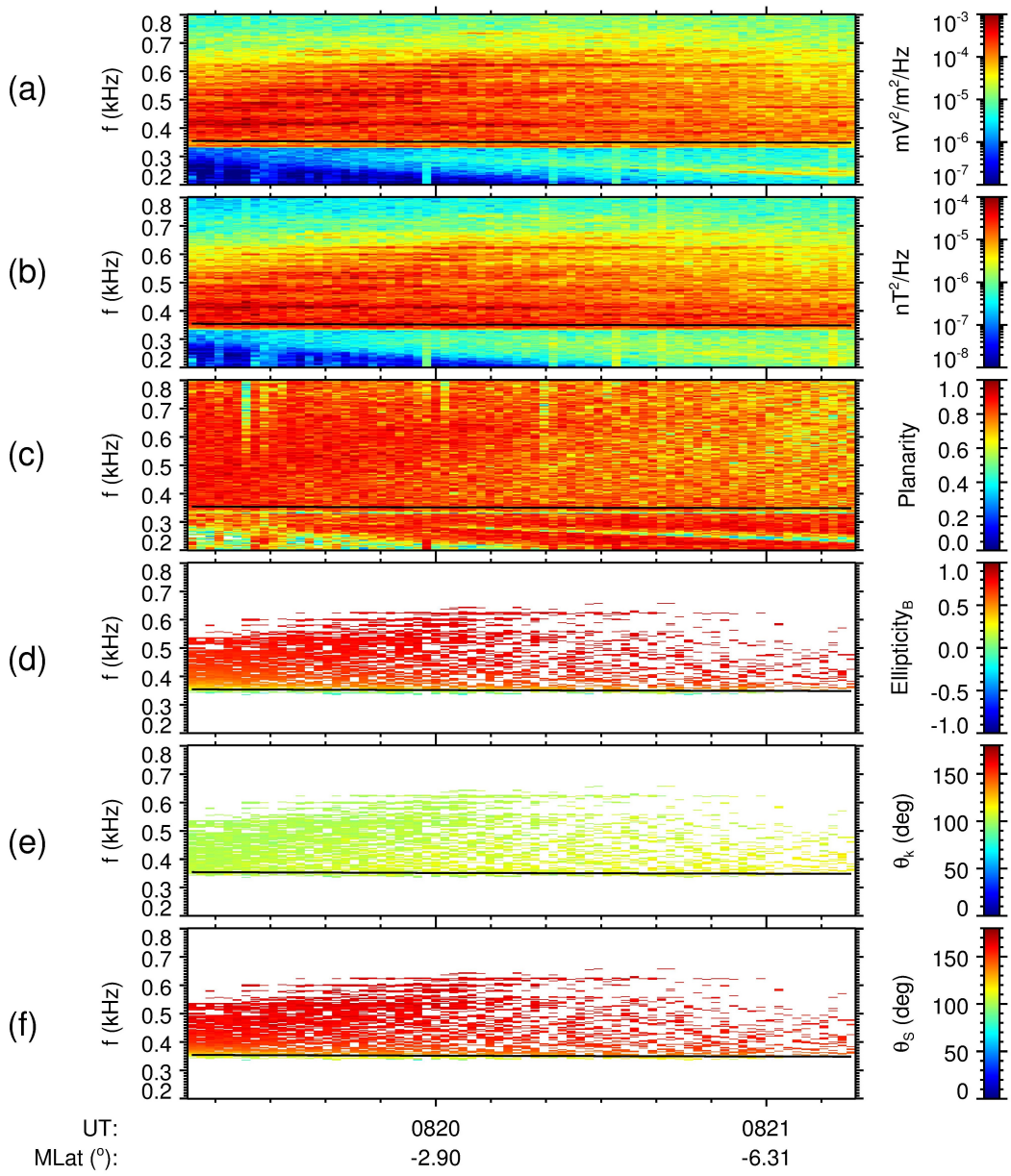

Figure 1. Time-frequency spectrograms showing wave properties of an equatorial noise event of 2004-11-09, 08:19:15 – 08:21:15 UT. a) Magnetic field PSD (Power Spectral Density), b) electric field PSD, c) planarity of polarization of the wave magnetic field, d) the ellipticity of polarization ellipse of the wave magnetic field, e) polar wave normal angle, f) polar angle of the Poynting vector. In panels d-f), magnetic field PSD and planarity thresholds are used to filter the data. The black line printed in all panels represents the local proton gyrofrequency.

In the analysis of wave propagation properties, we applied a threshold on the electric and magnetic power-spectral densities to remove other, weaker emissions. The values of the thresholds were selected manually for each event; in the example event, the values were $10^{-5}\,\mathrm{mV^2m^{-2}Hz^{-1}}$ and $10^{-5}\,\mathrm{nT^2Hz^{-1}}$. On top of that, a threshold of 0.8 on the values of planarity was applied in each of the observations. In Figures 1d–1f spectrograms of the three following wave properties are presented: ellipticity E_B (ratio of minor to major axis of the polarization ellipse of the wave magnetic field with the sign added based on the sense of polarization according to Santolík, Pickett, Gurnett, and Storey (2002)), wave normal angle θ_k (Santolík et al., 2003) and the polar angle of the Poynting vector θ_S (Santolík et al., 2010). We observe similar features in the spectrograms of θ_S and ellipticity, namely that both quantities attain their approximate maximum values of 180° (antiparallel propagation) and 1.0 (right-hand circular polarization) everywhere but in the region close to the local proton gyrofrequency f_cp. Here the Poynting vector becomes perpendicular to the magnetic field, and the polarization changes from right-hand circular to almost linear. The value of the wave normal angle is about 100° close to the equator for all frequencies and slightly increases its value as the spacecraft moves toward the southern hemisphere.

In the following statistical analysis, all data with wave frequencies below f_cp were excluded. This filter was added because the dispersion and polarization properties of the oblique whistler mode change rapidly below this characteristic frequency (Santolík et al., 2016), which would complicate further investigation of the results. Also, the dipole geomagnetic latitude λ_m was replaced by λ_Bmin, the geomagnetic latitude centered to the geomagnetic equator, which is defined by the minimum of the Earth's magnetic field along a field line. The minimum was obtained from the International Geomagnetic Reference Field (IGRF) and T89 magnetic field models (Tsyganenko, 1989).

2.2 Statistical Results

From all 46 equatorial noise events detected on DEMETER we constructed the distributions of θ_k, θ_S and E_B in geomagnetic latitudes, which we show in Figures 2a-c. In these plots, each dot represents one time-frequency bin of the associated spectrogram, and the individual events are differentiated by color. The EN statistic shows that beyond 22° of latitude, no equatorial noise emissions were observed. In the region within a few degrees of latitude from the equator, the waves propagate perpendicularly ($\theta_\mathrm{k} \approx$

90°) with low positive values of ellipticity, implying highly elliptical right-hand polarization. With increasing latitude, the wave normal angle deviates from the perpendicular direction with an almost linear trend. This is supported by the linear least squares fit in Figure 2a with a slope of -1.08 ($R^2 = 0.71$), which goes through 90° at the equator and reaches about 110° and 70° at $\lambda_{\mathrm{Bmin}} = -20°$ and $\lambda_{\mathrm{Bmin}} = 20°$, respectively. Ellipticity reflects this trend, becoming increasingly more circular further from the equator. The polar angle of the Poynting vector is centered around 90° at low latitudes but exhibits large variance. At higher latitudes, the Poynting vector becomes nearly parallel in the northern hemisphere and nearly antiparallel in the southern hemisphere, which means that when the waves crossed the altitude of DEMETER, they were propagating along the field lines and away from the equator.

The occurrence rate of EN events is plotted in Figure 2d as a function of the magnetic latitude. To obtain the occurrence rate, we considered each event as a box function equal to one inside the latitudinal interval where it was observed and zero everywhere else. These functions were then summed and normalized by the burst mode coverage (total number of half-orbits). All but one event are confined to the latitudinal interval $-20° < \lambda_{\mathrm{m}} < 20°$ and 75 % of the normalized occurrence falls within ±9 degrees of latitude from the magnetic equator. Figure 2e presents a histogram of the frequency extent of EN events; here, the events are again treated as box functions. For comparison, we overplotted in blue the same distribution with each measurement normalized to f_{cp}. The axes are scaled such that $1.0 f/f_{\mathrm{cp}}$ corresponds to wave frequency $f =$ 321 Hz, which is the average proton gyrofrequency over all EN events. The histogram in Figure 2f reveals that most of the events were recorded during times of enhanced geomagnetic activity. The geomagnetic activity is quantified by the 3-hour Kp index, which ranges from 2 to 8+ with an average value of 5. However, since high Kp indices are much less probable than the low ones (see the blue line in Figure 2f), we can deduce that the probability of occurrence of low altitudinal EN events increases rapidly with increasing Kp. The connection between enhanced geomagnetic activity and EN emissions propagating to low altitudes was previously noticed by Němec et al. (2016) and Santolík et al. (2016).

Based on the presented wave analysis, we picture the propagation of EN emissions as follows: During periods of enhanced geomagnetic activity, ion Bernstein modes are generated in the magnetosphere around the plasmapause region (Němec, Santolík, Pick-

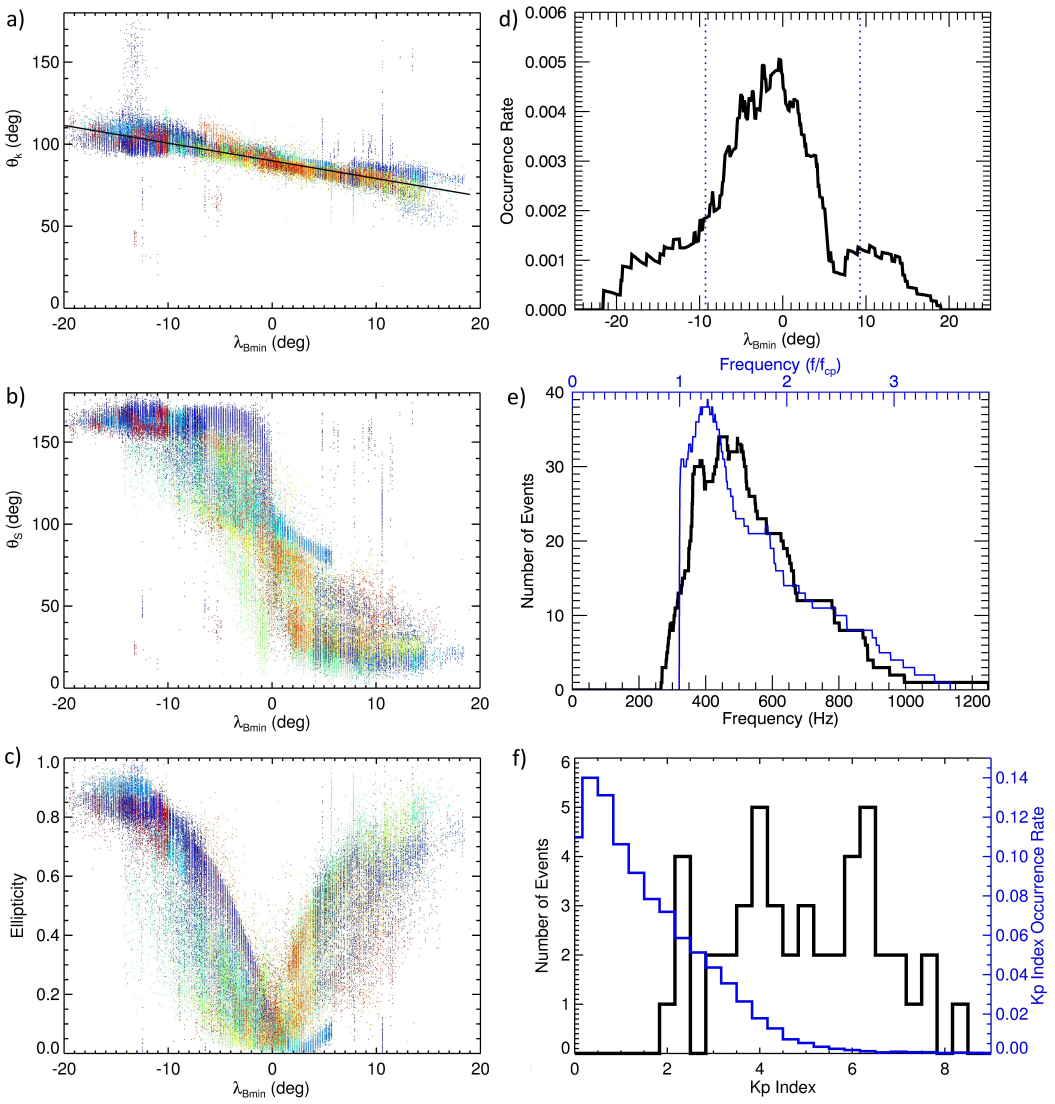

Figure 2. a) Wave normal angle. Each point represents one time-frequency bin in the corresponding spectrogram, each color represents one event. Black line shows the least square fit with the resulting linear term coefficient of −1.08. c) Polar angle of the Poynting vector, same plot format. b) Ellipticity of the magnetic field, same plot format. d) Latitudinal distribution of events normalized to the total number of DEMETER half-orbits with burst coverage. Blue dotted lines give the symmetric interval in which falls 75 % of the events. e) In black: Histogram of frequency distribution in hertz. In blue: Histogram of frequency distribution normalized to local proton gyrofrequency. Value of 1 on the upper axis corresponds to the average f_{cp} of 321 Hz on the bottom axis. f) In black: Histogram of geomagnetic activity distribution indicated by the Kp index. In blue: Occurrence rate of the values of Kp index during the whole operational period of the DEMETER spacecraft.

ett, Parrot, & Cornilleau-Wehrlin, 2013) and subsequently converted to the whistler wave mode. Due to their nearly perpendicular wave vectors, these modes propagate down to Earth through a region confined within a narrow range of latitudes (Boardsen et al., 1992; Hrbáčková et al., 2015). At low altitudes, the emissions cross the orbit of DEMETER. When the oscillations of the wave rays within the meridional plane are negligible, we observe perpendicular Poynting vectors close to the equator (see Figure 2b). Otherwise, we detect mainly quasiparallel Poynting vectors within a broader range of latitudes, with wave vectors appropriately tilted away from the perpendicular direction at higher latitudes. Waves with wave vectors deviating from the meridional plane are mostly deflected. The support for this EN propagation hypothesis is provided in the next sections through ray tracing simulations.

3 Ray Tracing Simulation

3.1 Methods and Models

To simulate the propagation of whistler-mode waves in a multicomponent cold plasma, we numerically solve 3D ray tracing equations with the 4th/5th order Dormand–Prince Runge–Kutta method from the SciPy Python library. The overall implementation is similar to the one found in Santolík et al. (2009), Section 2.3; the code and a quick guide can be downloaded from the link provided in the Open Research statement. We assume that the traversal of the plasmapause happens very early during the wave propagation so that the plasmapause can be excluded from our ray simulations. The model of electron density in the Earth's plasmasphere is adopted from Ozhogin et al. (2012), Equation 2. Only electrons and protons are included in this model. At radial distances between $1.3\,R_\mathrm{E}$ and $1.5\,R_\mathrm{E}$, Ozhogin's model is smoothly connected to the diffusive equilibrium (DE) model, which is shortly summarized in Bortnik et al. (2011), Equation 2 (for the original description of the diffusive equilibrium density model for the Earth's magnetosphere, see Angerami and Thomas (1964)). The two models are connected by cubic splines stretched along field lines. The values of DE model parameters, specified at the reference radial distance $h_0 = 660\,\mathrm{km}$ (the altitude of DEMETER), were chosen as follows: electron density $n_{\mathrm{e}0} = 3 \cdot 10^4\,\mathrm{cm}^{-3}$, ion temperature $T_{\mathrm{i}0} = 850\,\mathrm{K}$ and relative ion densities $\delta n_{\mathrm{p}0} = 0.25$ and $\delta n_{\mathrm{O}^+0} = 0.75$. According to the IRI model (Bilitza, 2018), these values are quite typical for dayside ionosphere at the equator during moderate or low solar activity. Any longitudinal variance in absolute or relative densities is

assumed to be negligible. The Earth's magnetic field is modeled by a perfect dipole, with the equatorial magnetic field strength at the surface set to $3.03{\cdot}10^{-5}$ T. The dipole geomagnetic latitude λ_{m} and the geomagnetic latitude centered to the minimum of the geomagnetic field λ_{Bmin} naturally coincide in this model.

While the ray tracing code is fully 3D and thus allows for azimuthal propagation, the next section focuses on purely meridional propagation, i.e., the initial azimuthal angle of the wave vector ϕ_{k0} is set to 180°. As we already mentioned in the introduction, it is unlikely that emissions propagating away from the initial meridional plane will reach the altitudes of DEMETER (Santolík et al., 2016). Nevertheless, to support this claim about preferential radial propagation, the effects of deviation of ϕ_{k0} from 180° are analyzed in Section 3.3.

3.2 Meridional Propagation

3.2.1 Simulation Setup

The initial values of ray parameters are based on our knowledge of the generation mechanism of EN and on the frequency histogram shown in Figure 2e. Source location at exactly $\lambda_{\mathrm{m}} = 0°$ is assumed, with radial distances ranging from $2.2\,R_{\mathrm{E}}$ to $3.2\,R_{\mathrm{E}}$ with a step of $0.05\,R_{\mathrm{E}}$. According to O'Brien and Moldwin (2003), the average plasmapause distance L_{pp} corresponds to the chosen source location for Kp indices from 6+ to 9−, but it should be noted that the L_{pp}(Kp) dependence displays a large variance. In addition, the simulated rays are assumed to start at the inner edge of the plasmapause and not at its center, thus further justifying the low values of initial radial distance.

With our magnetic field and density models, we can determine the range of equatorial lower hybrid frequencies $f_{\mathrm{lh}} = 580\,\mathrm{Hz}$ (largest initial distance) to $f_{\mathrm{lh}} = 1740\,\mathrm{Hz}$ (smallest initial distance). The L–cutoff of the whistler dispersion branch (Stix, 1992) calculated at the altitudes of DEMETER is approximately $f_{L=0} = 260\,\mathrm{Hz}$. We also know from our observations that there are no emissions observed above approximately 1200 Hz. With all these considerations in mind, we set the range of wave frequencies to 240 Hz – 1200 Hz spaced by 20 Hz, supplemented with the condition $f < f_{\mathrm{lh}}$.

The initial wave normal angles are chosen from the range $\theta_{\mathrm{k0}} = 85°$ to $\theta_{\mathrm{k0}} = 90°$ with a step of 0.1°. Due to the unknown hot proton distributions in the source region,

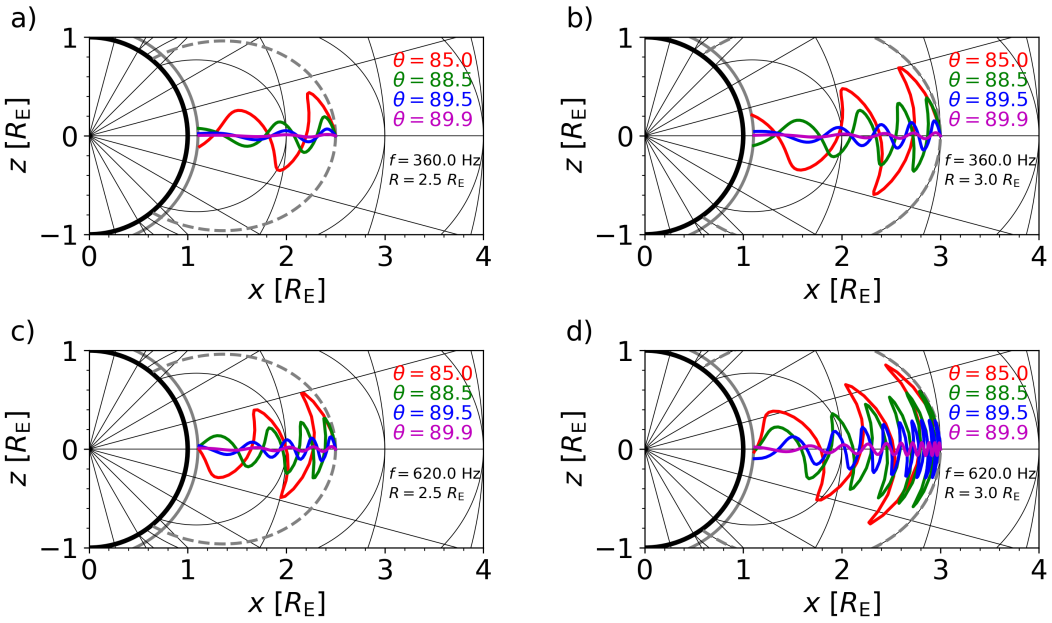

Figure 3. Propagation of selected rays with initial azimuthal angle $\phi_{k0} = 180°$. The grey dashed line represents the initial L-shell of traced rays, the solid grey arc marks the orbital altitude of DEMETER. Thin black lines represent radial distances (with a step of 1 R_E), latitudes (with a step of 15°) and L-shells (integer values). Individual ray trajectories are color-coded by their initial wave normal angle. Wave frequency and initial radial distance are given in each panel.

we cannot calculate the appropriate range of θ_{k0}, but based on linear growth calculations we can assume that the distribution should not be uniform but rather peaked around 90° (Chen, 2015; Min & Liu, 2016) – this issue will be addressed later in Section 3.2.3.

3.2.2 Ray Propagation Examples

The combination of input parameters and frequency limitations amounts to 49662 traced rays. As expected, all the rays with frequencies lower than the cutoff frequency $f_{L=0}$ at the altitudes of DEMETER were reflected, as well as most rays with frequencies 260 Hz and 280 Hz, which are still too close to the cutoff. At these low frequencies, the WKB (Wentzel-Kramers-Brillouin) condition was sometimes violated during the reflection, especially in cases with very low values of $|\theta_{k0} - 90°|$, reminding us of the limitations of the ray approximation.

In Figure 3 we show the resulting ray trajectories for some representative values of initial parameters. The initial L-shell and terminal altitude are marked by a dashed grey line and a solid grey line, respectively, and the coordinates λ_m, R and L are indicated by thin black lines. As the rays propagate down to Earth, their trajectories oscillate in latitude, where the amplitude of oscillations grows with the initial deviation of the wave normal angle, the initial distance, and the wave frequency. Higher frequency also leads to an increased number of equator crossings. Larger oscillation amplitudes may result in larger absolute values of final latitudes, but as shown in panel d), even wildly oscillating trajectories (red line, $\theta_{\mathrm{k}0} = 85°$) can arrive at the altitudes of DEMETER while crossing the magnetic equator. The latitudinal extent of the oscillations remains almost constant during the propagation.

3.2.3 Comparison with the Observations

For comparison of ray tracing results with experimental observations, we removed all rays with final f/f_cp ratio below 1, leaving us with 43028 rays in total (note that this condition leaves out the case studied by Santolík et al. (2016)). Furthermore, the symmetric trajectories with initial wave normal angles $90° - \theta_{\mathrm{k}0}$ are added, increasing the number of rays to 86056. 98.9 % of those reach the altitude of DEMETER. The simulated wave propagation properties are presented in Figure 4 as histograms of the incident ray count. The bin sizes are as follows: 0.5° in λ_m, 1° in θ_k and θ_S, and 0.05 in E_B. The latitudes are limited to the interval from −30° to 30°, into which falls 98.5 % of the rays that reached the terminal altitude.

Looking at the general trends, we can see that the wave normal angles (Figure 4a) increasingly deviate from 90° as the rays fall farther from the equator, and that the growth of the deviation has a mostly linear dependence on latitude. However, we notice that the spread of θ_k is considerably larger than in the experimental data. We quantify the trend by a linear fit (green dashed line), which now has a slope of −1.81, a much larger value compared to the slope of −1.08 calculated for the DEMETER data. The simulated Poynting vector angle θ_S also has the same general behavior as in the observational data, but most of the data points are concentrated near the parallel and antiparallel direction (more precisely, near 160° and 20°), with only 17 % of rays falling into the range from 45° to 135°. Similarly, the magnetic field ellipticity obtained through SVD methods (Santolík et al., 2003) also follows the trend set by the DEMETER data, but with a higher pref-

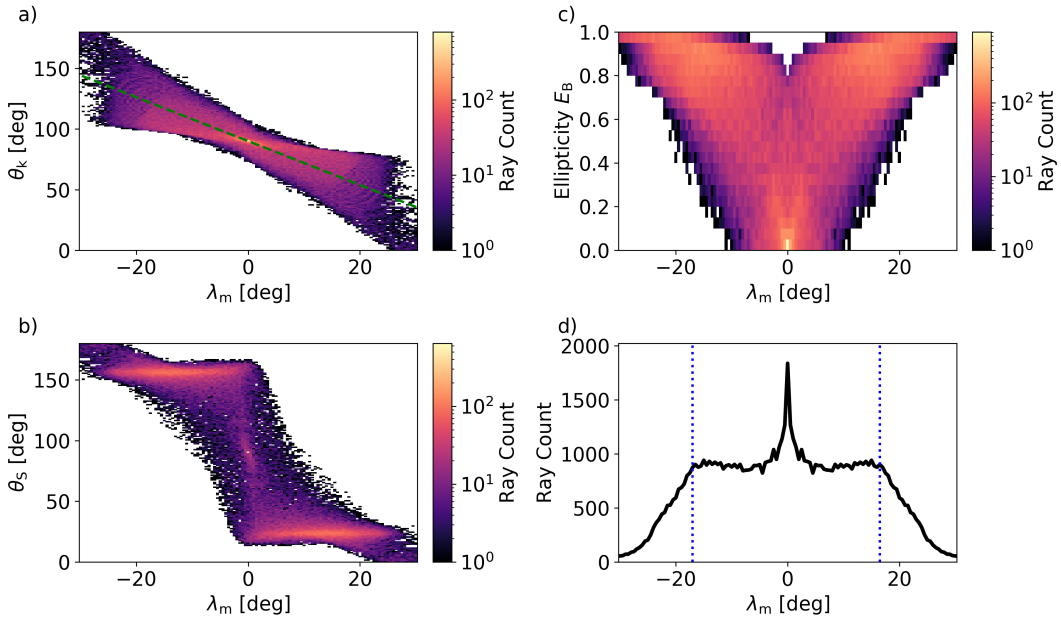

Figure 4. The same wave properties and distributions as in Figures 2a-d, plotted as histograms of the number of simulated rays reaching low altitudes. The green dashed line in panel a) is the linear least squares fit through all data points, with a slope of -1.81. In panel d) blue dotted lines give the $\pm 17°$ symmetric interval in which falls 75 % of the rays.

erence towards values above 0.5. The increase in E_B values happens at very low altitudes, while the distribution of ellipticity in the source region always remains concentrated near zero, in agreement with spacecraft observations (Santolík et al., 2004).

Overall, we showed a good qualitative agreement between the experiment and the simulation, confirming that the unusual properties of low altitude equatorial noise result from the propagation pattern of near-perpendicular whistler mode waves in the cold plasma of the plasmasphere. Nevertheless, there are noticeable discrepancies, which are probably best highlighted in panel d) of Figure 4, where we plot the distribution of incident rays across latitude. Apart from the sharp peak located right at the equator, the distribution is nearly uniform up to about $\lambda_m = 18°$, where it starts falling off. The blue dotted lines at $\pm 17°$ delimit the interval into which falls 75 % of rays, which is a marked increase from the $\pm 9°$ interval obtained with the DEMETER data. This increased spread in latitudes suggests that either the models we are using are not suitable or that the input values of the wave properties do not match the properties of the source of the equatorial noise.

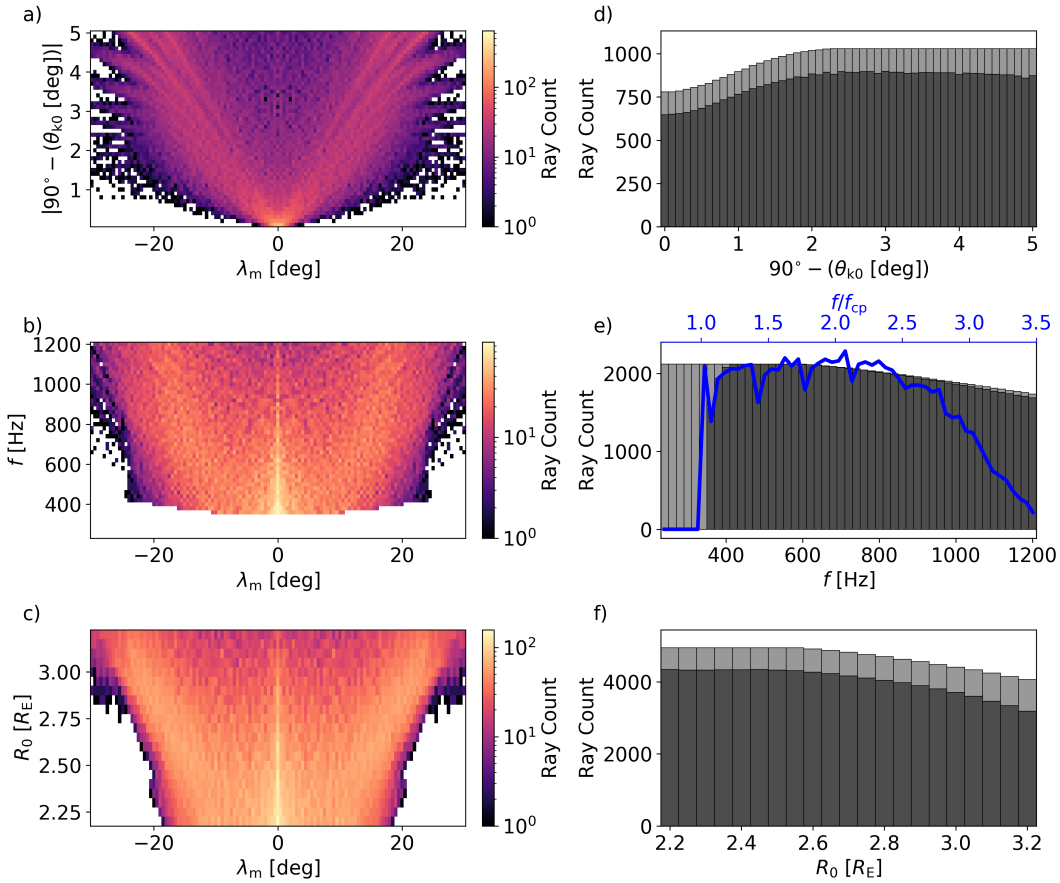

Figure 5. a-c) 2D histograms of incident rays in space of magnetic latitude and (a) initial wave normal angle θ_{k0}, (b) wave frequency f, and (c) polar angle of the Poynting vector θ_S. d-c) 1D histograms of the input parameters plotted in panels a-c). Light grey bars correspond to all initiated rays, dark grey bars represent only those rays which reached the altitude of DEMETER and had $f/f_{cp} > 1$ at the terminal point.

Leaving the question of the adequacy of magnetic field and density models for the discussion in Section 4, we now focus on modifying the set of input parameters. Figures 5a-c show similar histograms as Figures 4a-c, but the wave properties at low altitude are now replaced by the initial wave normal angle θ_{k0} (bin size 0.1°), wave frequency f (bin size 20 Hz) and initial radial distance (bin size 0.05 R_E). We make several observations based on these histograms. Firstly, all rays with θ_{k0} deviating less than ±0.7° from the perpendicular direction land within ±20° of the equator. Therefore, we must limit the initial spread in wave normal angles to improve the agreement between simulated and observed latitudinal distribution. Secondly, rays with large initial deviations follow a bi-modal distribution in latitudes, with only a small amount arriving near the equator. Rays with higher frequencies and larger initial distances also contribute predominantly to higher latitudes, but the dependence is less pronounced than in the case of θ_{k0}.

Figures 5d-f show the 1D histograms of the input ray parameters. Light grey histograms show the number of all rays that were started (not symmetrized in panel d), and the dark grey bars show the rays which arrived at the altitudes of DEMETER and satisfied the condition $f/f_{cp} > 1$. We notice that due to the lower hybrid resonance imposing an upper limit on the whistler mode frequencies, the number of rays decreases with θ_{k0} approaching 90°, which is exactly the opposite of what we would expect from a realistic source of EN. The histogram of frequencies shows a decreasing trend starting at 440 Hz, but the drop off is much slower than in the observed frequency distribution (Figure 2e) and is almost exclusively due to the lower hybrid resonance. Lastly, we show the histogram of initial radial distances, which also exhibits a downward trend associated with f_{lh}.

We now introduce a gaussian weighting function

$$w(\theta_{k0}; \sigma_\theta) = \exp\left(\frac{-(\theta_{k0} - 90°)^2}{2\sigma_\theta^2}\right) \tag{1}$$

to model the distribution of the initial wave normal angles. The initial frequency distribution is divided into 4 bins with edge values $[240, 480, 720, 960, 1200]$ Hz, and to each bin we assign a normalization factor a_i, $i \in \{1, 2, 3, 4\}$. The distribution of initial distances is not weighted but is indirectly influenced by the distribution of θ_{k0} and f through the cold plasma dispersion relation of the whistler mode. In total, we have 5 parameters (σ_θ, a_1, a_2, a_3, a_4) which are determined by the nonlinear least squares fit of the

histogram of the latitude of incident rays to the occurrence plot in Figure 2d. For the purpose of the fitting procedure, the experimental data are rebinned to λ_{Bmin} bins of 0.5°.

The optimal parameters were found with the Levenberg–Marquardt algorithm (as implemented in SciPy, Moré (1978)). Because it does not ensure that global minima will be found, we tried five different guesses of σ_θ, increasing from 1° to 5° with a step of 1°. The frequency distribution normalization factors were set to $a_1 = 1.0$, $a_2 = 1.0$, $a_3 = 0.25$ and $a_4 = 0.0625$, approximately following the distribution obtained from the DEMETER data. The resulting best fit parameters are: $\sigma_\theta = 2.01°$, $a_1 = 0.59$, $a_2 = 0.37$, $a_3 = 0.0$ and $a_4 = 0.040$ (sum of a_i has been normalized to 1). The histograms from Figure 4 are recalculated with the obtained weights and presented in Figure 6. The quantitative agreement between simulation and experiment has clearly improved, as shown by the decrease in the slope of the linear fit of θ_{k} data from -1.81 to -1.60, and by the narrowing of the occurrence histogram in latitudes. 75 % of the rays now fall within ±10° around the equator, which almost matches the experimental value of ±9°. Extreme values of all three wave propagation parameters θ_{k}, θ_{S} and E_{B} are now overall less pronounced.

An alternative option of keeping a_i fixed and fitting only the standard deviation of θ_{k0} distribution results in $\sigma_\theta = 1.42°$ and the linear fit of $\theta_{\mathrm{k}}(\lambda_{\mathrm{m}})$ then has a slope of -1.50. However, the simulated frequency histogram then does not match the experimental results and the sum of squares of residuals increases. Ideally, we should try to minimize the residuals not only for the experimental distribution of latitudes in Figure 2d, but across all experimental histograms in Figures 2a-e; unfortunately, there is no reliable method that would prescribe a weight or importance to each histogram.

3.3 Azimuthal Propagation

3.3.1 Simulation Setup

Apart from the meridional propagation of the large set of rays, we also present the 3D tracing of another, smaller set of rays with azimuthal angles ranging from 170.0° to 179.8° (step 0.2°). The other wave parameters are restricted followingly: θ_{k} goes from 88.50° to 89.95° (step 0.05°), frequencies are set to 360 Hz and 620 Hz and radial distances to 2.5 R_{E} and 3.0 R_{E}. In total, 6000 rays were traced. The questions we aim to resolve with this simulation are these: for which values of the initial azimuthal angle ϕ_{k0}

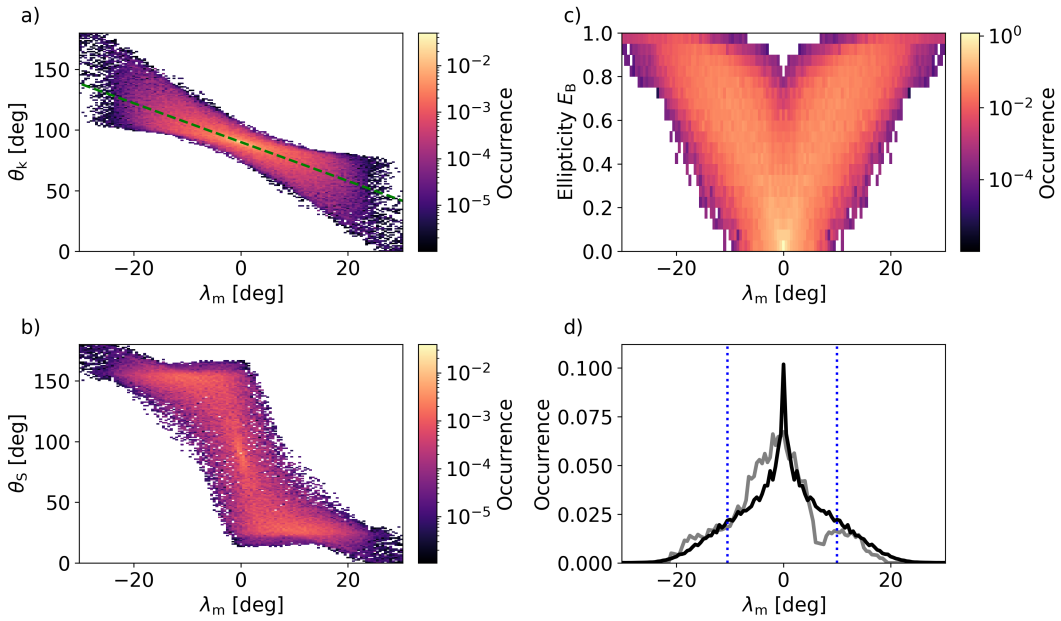

Figure 6. Histograms of the number of incident rays. Same types of plots as in Figure 4, but with weighting functions imposed in the initial ray tracing parameters according to a nonlinear least squares method (see text). Linear fit through the wave normal angles against latitudes in panel a) has a slope of −1.60. In panel d), the experimental occurrence of low altitude noise is overplotted in grey, and the 75 % symmetric interval is shown by vertical blue dotted lines.

can the rays reach DEMETER, and how do the final values of λ_m, θ_k and longitude depend on the choice of ϕ_{k0}.

3.3.2 Ray Propagation Statistics

In Figure 7 we show 2D plots of terminal wave normal angles, latitudes and longitudes in (θ_{k0},ϕ_{k0}) space. First, let us look at the behavior of the plots for $\phi_{k0} > 179°$. As the deviation of θ_{k0} from 90° increases, the latitudes and wave normal angles at the altitudes of DEMETER start to oscillate. The oscillations become faster and more pronounced as the distance and frequency increase; this is similar to the observations made on ray trajectories plotted in Figure 3. The terminal longitude is nearly independent of the initial wave normal angle, and its value remains near 0° (in the same magnetic meridian as the source), with only a slight increase with frequency and initial distance.

As we move to $\phi_{k0} < 179°$, the behavior changes. The oscillations in the latitudes and wave normal angles slightly increase in amplitude, and the rays can reach longitudes of up to about 50° from the source magnetic meridian. At a certain point, due to the azimuthal component of the wave vector increasing, the rays experience reflection before reaching the desired altitude. The minimum ϕ_{k0} which enables crossing of the ray trajectory with the altitude of DEMETER is approximately 174° for $f = 360\,\mathrm{Hz}$ and $R_0 = 2.5\,R_E$ and shows almost no dependence on θ_{k0}. On the other hand, rays started at $R_0 = 3.0\,R_E$ with frequency $f = 620\,\mathrm{Hz}$ are limited to $\phi_{k0} > 178°$ for $\theta_{k0} = 89.95°$, and the interval of ϕ_{k0} increases with the deviation of the initial wave normal angle from 90° up to $\phi_{k0} > 177°$ for $\theta_{k0} = 88.50°$. We have thus proven that the equatorial noise can reach DEMETER only when the initial deviation from the radial direction in azimuth is only a few degrees or less, and the limit decreases rapidly with wave frequency and initial distance. Moreover, the MLT of the observation can reach over 2 hours from the source location only with ϕ_{k0} very close to the deflection threshold. These findings justify our approach from Section 2 where the experimental data were compared to results obtained from ray propagation restricted to the meridional plane.

Our findings on longitudinal propagation and ray deflection can be compared with an analytic estimate of the lowest altitude reached by the rays based on the conservation of the geometric invariant

$$Q = \mu R \sin\phi_S \,. \tag{2}$$

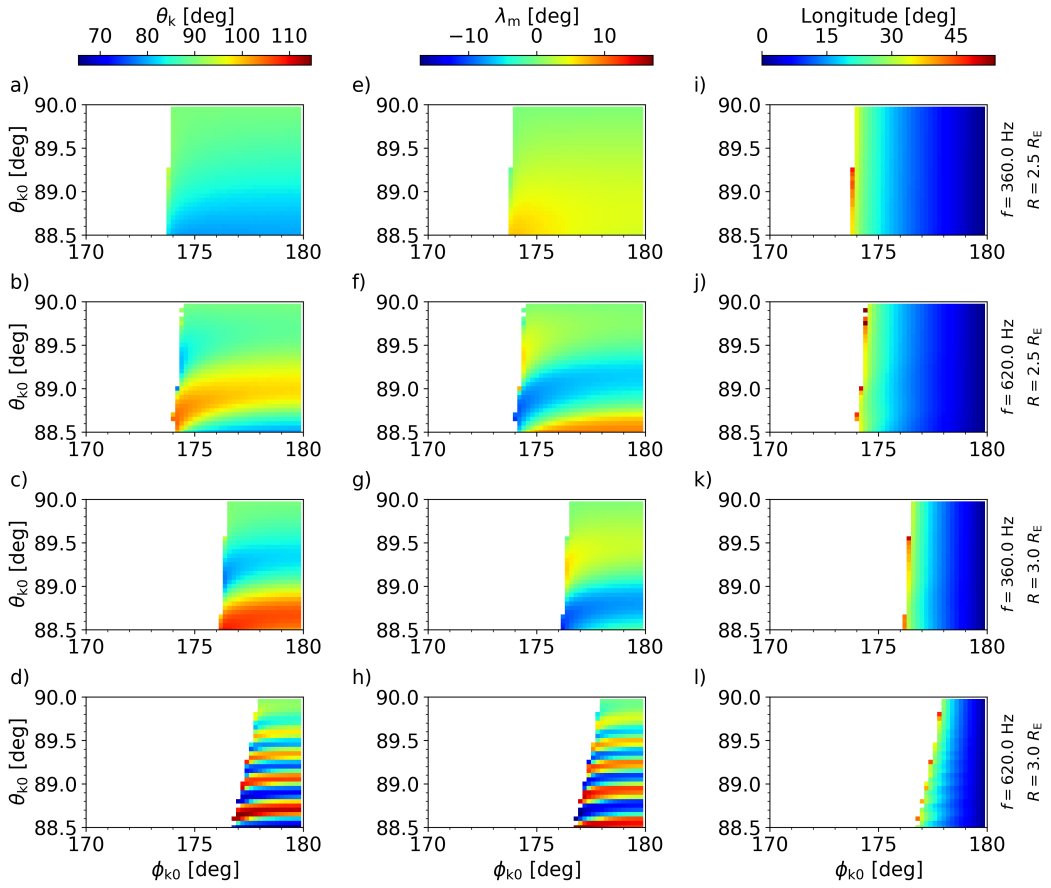

Figure 7. a-d) Wave normal angles of simulated rays after reaching the altitude of DEMETER, plotted as a function of the initial wave normal angle θ_{k0} and the initial azimuthal angle ϕ_{k0}. e-h) Latitude where rays crossed the altitude of DEMETER, same plot format as in a-d). i-l) Longitude where rays crossed the altitude of DEMETER, same plot format as in a-d). On the right side of the figure, initial radial distances and wave frequencies are indicated for each triplet of plots.

Here, μ denotes the refractive index and ϕ_S is the azimuthal deviation angle of the Poynting vector from the direction towards the Earth's surface. For Q to be truly invariant, the propagation medium must be axially symmetric, and the ray trajectories must lie in the equatorial plane (for more details, see Chen and Thorne (2012), Section 2). Therefore, we can analyze only waves with a constant $\theta_k = 90°$ by this method. Notice that due to the axial symmetry of the plasma medium, the azimuthal angle of the Poynting vector and the wave vector coincide. By tracking the evolution of refractive index along the path of rays with $\theta_{k0} = 89.95°$, we can confirm that the values of ϕ_{k0} at which the rays start experiencing deflection from Earth matches the theoretical prediction. Because results presented in Figure 7 show that θ_{k0} does not have much impact on the range of ϕ_{k0} for lower values of frequency and R_0, Equation 2 can be used in these cases to determine which rays can reach the altitudes of low orbit spacecraft.

4 Discussion

In the analysis of electromagnetic data from DEMETER, we decided to remove all frequencies below the local proton gyrofreqency. That way, we completely excluded the event studied by Santolík et al. (2016) from our dataset. In this case study, the reported equatorial noise emission occurred within 10° of the equator, with θ_k very close to 90°, and at frequencies extending below $f_{cp}/2$. Dispersion properties at these frequencies strongly depend on the ion composition, which would increase the number of parameters in our analysis. Of all the frequency-time intervals with EN in our dataset, after applying the thresholds on power density and planarity, only 27.6 % fall under f_{cp}, and therefore we have chosen not to include this smaller, special part of the dataset in our analysis.

In the comparison of the ray tracing results with the experimental data (Section 3.2.3), we encountered some difficulties related to the choice of input and output parameters. We chose to compare the occurrence of equatorial noise in magnetic latitudes, but we could have chosen the occurrence in a two-dimensional space of latitude and a selected wave propagation property. Our decision was motivated by the fact that the total number of events is relatively low, so the 2D histograms might not be representative of the whole statistical population due to the larger space that needs to be sampled.

There is also no rigorous way to determine the optimal size of bins in the histogram, apart from the requirement that the total number of bins (output parameters) must be

larger than or equal to the number of the input parameters. We decided to keep the number of input parameters as low as reasonably possible, which is why the frequency distribution was divided only into four bins with a corresponding number of normalization factors. Unlike in the case of the θ_{k0} distribution, we do not have a model of the frequency distribution that could be described by an elementary function. The distribution in initial radial distances was not parametrized because the histogram of ray occurrence in the R_0 and λ_m space is very similar to the histogram in the f and λ_m space, and so it would be problematic to separate the influence of frequency on the occurrence in latitudes from the influence of the initial distance.

Despite the complexity of the relations between the various input and output parameters of the system, we achieved a solid agreement between the weighted latitudinal histogram and its experimental counterpart. Unfortunately, the sharp peak near $\lambda_m = 0°$ could not be removed by the weighting procedure. We hypothesize that the absence of this peak in the observational data comes from the simple fact that the source of EN is not located precisely at $\lambda_{Bmin} = 0°$, but has a small spread along the local field line which results in a smearing of the histogram.

The effects of the azimuthal component of the wave vector on the propagation of equatorial noise to low altitudes were studied previously by Santolík et al. (2016). Based on a ray tracing simulation, they concluded that the initial azimuthal angle must not deviate by more than 1° from the radial direction, and thus that only a small fraction of equatorial noise waves can propagate down to the DEMETER orbit. As we have shown in Figure 7, the available range of azimuth increases with decreasing initial radial distance and frequency. As long as the distribution of θ_{k0} is very narrow, Equation 2 gives a good estimate on the range of ϕ_{k0} for a given radial distance of the source; however, the initial distance cannot be reliably estimated from the line spectrum, because in most cases, the spectrograms feature overlapping lines associated with multiple sources acting at different radial distances at the same time.

Some aspects of the propagation of equatorial noise were omitted entirely from our ray tracing analysis. First, we decided to use a single model of the ionosphere instead of dividing the simulation models into ray propagation during day and night. This choice is acceptable as long as we ignore the waves below proton gyrofrequency. Otherwise, the density ratio of oxygen to hydrogen ions would play a significant role in the computa-

tion of the refractive index at the low frequency part of the EN emission spectrum, and as was shown by the ion measurements from DEMETER (Gladyshev et al., 2012), or as predicted by the IRI model (Bilitza, 2018), the ion composition varies as a function of MLT. It also depends on the latitude, but this becomes important only at higher latitudes. And second, the ray propagation depends on the model of plasmaspheric electron density. We expect that the density gradient along field lines can influence the spread of EN occurrence in latitudes and the wave propagation properties observed on DEMETER.

5 Conclusion

We analyzed electromagnetic wave data of low-altitudinal equatorial noise emissions measured during the whole mission of the DEMETER spacecraft and presented the statistics of wave propagation properties of those emissions, namely wave normal angle, polar angle of the Poynting vector, the ellipticity of polarization, latitudinal distribution and frequency distribution. The emissions are observed within about 20° of the geomagnetic equator with wave normal angles mostly between 60° and 120°, while the polar angle of the Poynting vector ranges across the whole range from 0° to 180°, with the very high and very low values being dominant farther from the equator. We have also confirmed that the occurrence of these emissions is accompanied by strong geomagnetic activity, as was indicated earlier by Němec et al. (2016).

Comparison of the observational data with a numerical ray tracing experiment confirms that the observation is in good agreement with the theory of wave propagation in cold plasma under suitable assumptions about the nature of the source region. We also showed that the possible initial azimuthal angles are limited to only a few degrees around the radial downward direction, and this interval decreases with growing frequency and initial radial distance. This behavior explains why the equatorial noise can be observed at low altitudes predominantly in periods of very high geomagnetic activity, during which the source region probably moves closer to the Earth.

The analysis presented in this paper could be improved by acquiring simultaneous measurements of EN and hot proton distributions in the source region and consequent calculation of growth rates, providing thus solid support for the choice of initial wave properties. Also, a larger experimental dataset could reveal more detailed features of the sta-

tistical behavior of wave propagation parameters. Furthermore, we left open the question of the effect of the electron density model on the propagation properties of the equatorial noise emissions, and we did not address the behavior of the part of the emission reaching below the local proton gyrofrequency. These points will be investigated in future studies.

Open Research

DEMETER spacecraft data are accessible from `https://sipad-cdpp.cnes.fr`. The processed equatorial noise data used in this paper and related IDL procedures can be found at `https://doi.org/10.6084/m9.figshare.19208646.v1`. Kp indices can be downloaded from the World Data Center for Geomagnetism, Kyoto `http://wdc.kugi.kyoto-u.ac.jp/dstae/index.html`. The ray tracing code and associated input files and Python plotting procedures can be found at `https://doi.org/10.6084/m9.figshare.19181864.v1`.

Acknowledgments

This work has received funding from the European Union's Horizon 2020 research and innovation programme under grant agreement No. 870452 (PAGER). The work of MH and OS was supported from the GA UK project No. 64120. The work of FN was supported from the GACR project No. 21-01813S. We thank the engineers from CNES and scientific laboratories (CBK, IRAP, LPC2E, LPP, and SSD of ESTEC) who largely contributed to the success of the DEMETER spacecraft mission.

References

Angerami, J. J., & Thomas, J. O. (1964, November). Studies of Planetary Atmospheres, 1, The Distribution of Electrons and Ions in the Earth's Exosphere. *J. Geophys. Res.*, *69*, 4537-4560. doi: 10.1029/JZ069i021p04537

Berthelier, J. J., Godefroy, M., Leblanc, F., Malingre, M., Menvielle, M., Lagoutte, D., ... Pfaff, R. (2006, April). ICE, the electric field experiment on DEMETER. *Planet. Space Sci.*, *54*, 456-471. doi: 10.1016/j.pss.2005.10.016

Bilitza, D. (2018, September). IRI the International Standard for the Ionosphere. *Adv. Radio Sci.*, *16*, 1-11. doi: 10.5194/ars-16-1-2018

Boardsen, S. A., Gallagher, D. L., Gurnett, D. A., Peterson, W. K., & Green, J. L.

(1992, October). Funnel-shaped, low-frequency equatorial waves. *J. Geophys. Res. Space Physics*, *97*, 14967-14976. doi: 10.1029/92JA00827

Boardsen, S. A., Hospodarsky, G. B., Kletzing, C. A., Engebretson, M. J., Pfaff, R. F., Wygant, J. R., ... De Pascuale, S. (2016, April). Survey of the frequency dependent latitudinal distribution of the fast magnetosonic wave mode from Van Allen Probes Electric and Magnetic Field Instrument and Integrated Science waveform receiver plasma wave analysis. *J. Geophys. Res. Space Physics*, *121*, 2902-2921. doi: 10.1002/2015JA021844

Bortnik, J., Chen, L., Li, W., Thorne, R. M., & Horne, R. B. (2011, August). Modeling the evolution of chorus waves into plasmaspheric hiss. *J. Geophys. Res. Space Physics*, *116*, A08221. doi: 10.1029/2011JA016499

Chen, L. (2015, June). Wave normal angle and frequency characteristics of magnetosonic wave linear instability. *Geophys. Res. Lett.*, *42*, 4709-4715. doi: 10.1002/2015GL064237

Chen, L., & Thorne, R. M. (2012, July). Perpendicular propagation of magnetosonic waves. *Geophys. Res. Lett.*, *39*, L14102. doi: 10.1029/2012GL052485

Gladyshev, V. A., Shchekotov, A. Y., Yagova, N. V., Berthelier, J. J., Parrot, M., Akent'eva, O. S., ... Molchanov, O. A. (2012, April). Concentration of ions in the topside ionosphere as measured onboard the DEMETER satellite: Morphology and dependence on solar and geomagnetic activity. *Cosmic Research*, *50*(2), 103-115. doi: 10.1134/S0010952512020037

Gurnett, D. A. (1976, June). Plasma wave interactions with energetic ions near the magnetic equator. *J. Geophys. Res.*, *81*, 2765. doi: 10.1029/JA081i016p02765

Horne, R. B., Thorne, R. M., Glauert, S. A., Meredith, N. P., Pokhotelov, D., & Santolík, O. (2007, September). Electron acceleration in the Van Allen radiation belts by fast magnetosonic waves. *Geophys. Res. Lett.*, *34*(17), L17107. doi: 10.1029/2007GL030267

Horne, R. B., Wheeler, G. V., & Alleyne, H. S. C. K. (2000, December). Proton and electron heating by radially propagating fast magnetosonic waves. *J. Geophys. Res. Space Physics*, *105*, 27597-27610. doi: 10.1029/2000JA000018

Hrbáčková, Z., Santolík, O., Němec, F., Macúšová, E., & Cornilleau-Wehrlin, N. (2015, February). Systematic analysis of occurrence of equatorial noise emissions using 10 years of data from the Cluster mission. *J. Geophys. Res. Space*

Physics, *120*, 1007-1021. doi: 10.1002/2014JA020268

Kasahara, Y., Kenmochi, H., & Kimura, I. (1994, July). Propagation characteristics of the ELF emissions observed by the satellite Akebono in the magnetic equatorial region. *Rad. Sci.*, *29*(4), 751-767. doi: 10.1029/94RS00445

Liu, K., Gary, S. P., & Winske, D. (2011, July). Excitation of magnetosonic waves in the terrestrial magnetosphere: Particle-in-cell simulations. *J. Geophys. Res. Space Physics*, *116*, A07212. doi: 10.1029/2010JA016372

Ma, Q., Li, W., Chen, L., Thorne, R. M., & Angelopoulos, V. (2014, February). Magnetosonic wave excitation by ion ring distributions in the Earth's inner magnetosphere. *J. Geophys. Res. Space Physics*, *119*, 844-852. doi: 10.1002/2013JA019591

Ma, Q., Li, W., Thorne, R. M., & Angelopoulos, V. (2013, May). Global distribution of equatorial magnetosonic waves observed by THEMIS. *Geophys. Res. Lett.*, *40*, 1895-1901. doi: 10.1002/grl.50434

Meredith, N. P., Horne, R. B., & Anderson, R. R. (2008, June). Survey of magnetosonic waves and proton ring distributions in the Earth's inner magnetosphere. *J. Geophys. Res. Space Physics*, *113*, A06213. doi: 10.1029/2007JA012975

Min, K., & Liu, K. (2016, April). Understanding the growth rate patterns of ion Bernstein instabilities driven by ring-like proton velocity distributions. *J. Geophys. Res. Space Physics*, *121*, 3036-3049. doi: 10.1002/2016JA022524

Moré, J. J. (1978). The Levenberg-Marquardt algorithm: Implementation and theory. In G. A. Watson (Ed.), *Numerical Analysis* (pp. 105–116). Berlin, Heidelberg: Springer Berlin Heidelberg.

Němec, F., Parrot, M., & Santolík, O. (2016, October). Equatorial noise emissions observed by the DEMETER spacecraft during geomagnetic storms. *J. Geophys. Res. Space Physics*, *121*, 9744-9757. doi: 10.1002/2016JA023145

Němec, F., Santolík, O., Parrot, M., & Berthelier, J. J. (2007, April). Comparison of magnetospheric line radiation and power line harmonic radiation: A systematic survey using the DEMETER spacecraft. *J. Geophys. Res. Space Physics*, *112*, A04301. doi: 10.1029/2006JA012134

Němec, F., Santolík, O., Pickett, J. S., Hrbáčková, Z., & Cornilleau-Wehrlin, N. (2013, November). Azimuthal directions of equatorial noise propagation de-

termined using 10 years of data from the Cluster spacecraft. *J. Geophys. Res. Space Physics*, *118*, 7160-7169. doi: 10.1002/2013JA019373

Němec, F., Santolík, O., Pickett, J. S., Parrot, M., & Cornilleau-Wehrlin, N. (2013, July). Quasiperiodic emissions observed by the Cluster spacecraft and their association with ULF magnetic pulsations. *J. Geophys. Res. Space Physics*, *118*, 4210-4220. doi: 10.1002/jgra.50406

O'Brien, T. P., & Moldwin, M. B. (2003, February). Empirical plasmapause models from magnetic indices. *Geophys. Res. Lett.*, *30*, 1-1. doi: 10.1029/2002GL016007

Ozhogin, P., Tu, J., Song, P., & Reinisch, B. W. (2012, June). Field-aligned distribution of the plasmaspheric electron density: An empirical model derived from the IMAGE RPI measurements. *J. Geophys. Res. Space Physics*, *117*, A06225. doi: 10.1029/2011JA017330

Parrot, M., Benoist, D., Berthelier, J. J., Błęcki, J., Chapuis, Y., Colin, F., ... Zamora, P. (2006, April). The magnetic field experiment IMSC and its data processing onboard DEMETER: Scientific objectives, description and first results. *Planet. Space Sci.*, *54*, 441-455. doi: 10.1016/j.pss.2005.10.015

Perraut, S., Roux, A., Robert, P., Gendrin, R., Sauvaud, J. A., Bosqued, J. M., ... Korth, A. (1982, August). A systematic study of ULF waves above F_{H^+} from GEOS 1 and 2 measurements and their relationships with proton ring distributions. *J. Geophys. Res.*, *87*, 6219-6236. doi: 10.1029/JA087iA08p06219

Posch, J. L., Engebretson, M. J., Olson, C. N., Thaller, S. A., Breneman, A. W., Wygant, J. R., ... Reeves, G. D. (2015, August). Low-harmonic magnetosonic waves observed by the Van Allen Probes. *J. Geophys. Res. Space Physics*, *120*(8), 6230-6257. doi: 10.1002/2015JA021179

Russell, C. T., Holzer, R. E., & Smith, E. J. (1970, January). OGO 3 observations of ELF noise in the magnetosphere: 2. The nature of the equatorial noise. *J. Geophys. Res.*, *75*, 755. doi: 10.1029/JA075i004p00755

Santolík, O., Nemec, F., Gereová, K., Macúšová, E., Conchy, Y., & Cornilleau-Wehrlin, N. (2004, July). Systematic analysis of equatorial noise below the lower hybrid frequency. *Ann. Geophys.*, *22*, 2587-2595. doi: 10.5194/angeo-22-2587-2004

Santolík, O., Němec, F., Parrot, M., Lagoutte, D., Madrias, L., & Berthelier, J. J.

(2006, April). Analysis methods for multi-component wave measurements on board the DEMETER spacecraft. *Planet. Space Sci.*, *54*, 512-527. doi: 10.1016/j.pss.2005.10.020

Santolík, O., Parrot, M., Inan, U. S., Burešová, D., Gurnett, D. A., & Chum, J. (2009, March). Propagation of unducted whistlers from their source lightning: A case study. *J. Geophys. Res. Space Physics*, *114*, A03212. doi: 10.1029/2008JA013776

Santolík, O., Parrot, M., & Lefeuvre, F. (2003, February). Singular value decomposition methods for wave propagation analysis. *Rad. Sci.*, *38*, 10-1. doi: 10.1029/2000RS002523

Santolík, O., Parrot, M., & Němec, F. (2016, July). Propagation of equatorial noise to low altitudes: Decoupling from the magnetosonic mode. *Geophys. Res. Lett.*, *43*, 6694-6704. doi: 10.1002/2016GL069582

Santolík, O., Pickett, J. S., Gurnett, D. A., Maksimovic, M., & Cornilleau-Wehrlin, N. (2002, December). Spatiotemporal variability and propagation of equatorial noise observed by Cluster. *J. Geophys. Res. Space Physics*, *107*(A12), 1495. doi: 10.1029/2001JA009159

Santolík, O., Pickett, J. S., Gurnett, D. A., Menietti, J. D., Tsurutani, B. T., & Verkhoglyadova, O. (2010, July). Survey of Poynting flux of whistler mode chorus in the outer zone. *J. Geophys. Res. Space Physics*, *115*, A00F13. doi: 10.1029/2009JA014925

Santolík, O., Pickett, J. S., Gurnett, D. A., & Storey, L. R. O. (2002, Dec). Magnetic component of narrowband ion cyclotron waves in the auroral zone. *J. Geophys. Res. Space Physics*, *107*(A12), 1444. doi: 10.1029/2001JA000146

Stix, T. (1992). *Waves in Plasmas*. Melville NY: American Institute of Physics.

Tsyganenko, N. A. (1989, January). A magnetospheric magnetic field model with a warped tail current sheet. *Planet. Space Sci.*, *37*, 5-20. doi: 10.1016/0032-0633(89)90066-4

Xiao, F., Zhou, Q., He, Z., Yang, C., He, Y., & Tang, L. (2013, July). Magnetosonic wave instability by proton ring distributions: Simultaneous data and modeling. *J. Geophys. Res. Space Physics*, *118*, 4053-4058. doi: 10.1002/jgra.50401